

Cite this: *Energy Environ. Sci.*,
2022, 15, 1529

Creation of a rigid host framework with optimum crystal structure and interface for zero-strain K-ion storage†

Yun-Hai Zhu,[†] Jia-Zhi Wang,[‡] Qi Zhang,^b Yang-Feng Cui,^{bd} Gang Huang,^b Jun-Min Yan,[†] and Xin-Bo Zhang^{†*}

Potassium-ion batteries (KIBs) have gained considerable attention for stationary energy storage devices due to their low cost, natural abundance, and high energy density. However, owing to the significant strain caused by the accommodation of K ions, the diffusion of large K ions into conventional host frameworks inevitably causes sluggish diffusion kinetics or even structural failure during repeated K-ion insertion/extraction. Herein, to counter the mismatched relationship between the large K ions and compact host structures, we propose a new host design strategy that combines crystal engineering with interface engineering. Taking layered KTiNbO_5 (KTNO) as an example, favorable and stable K-ion diffusion channels are constructed in the rigid host through topologically converting layered KTNO into tunnel-structured $\text{Ti}_2\text{Nb}_2\text{O}_9$ (TNO) that stores K ions in a zero-strain way. Additionally, to overcome the limitation of K-ion storage sites inside a crystal, TNO is then exfoliated into nanosheets and further *in situ* coated with a highly graphitized carbon layer (CTNO). The resultant heterogeneous interfaces compensate for the unsaturated coordination environment of the TNO external surface and consequently provide abundant K-ion storage sites. Benefiting from the tailored crystal structures and heterogeneous interfaces, CTNO exhibits high reversible capacity ($\sim 205 \text{ mA h g}^{-1}$), excellent rate capability ($\sim 72\%$ capacity retention at 8 A g^{-1}), and remarkable lifespan ($\sim 100\%$ capacity retention across nearly 10 000 cycles). These findings demonstrate the great potential of CTNO as a KIB material and provide insights into host design for achieving fast K-ion storage toward practical applications.

Received 19th December 2021,
Accepted 10th February 2022

DOI: 10.1039/d1ee03924e

rsc.li/ees

Broader context

To respond to the energy crisis and environmental pollution driven by increasing global energy consumption, various energy storage technologies that integrate renewable energies into the smart grid and electronic vehicles are emerging rapidly. Among them, potassium-ion batteries (KIBs) provide the greatest opportunities to meet the needs for scalable and affordable stationary applications, due to the abundance and low cost of natural potassium resources. However, the dauntingly large size of the K ion (1.3 \AA) makes its diffusion kinetics extremely slow or even impossible in crystalline solids, and thus state-of-the-art KIBs suffer from low capacity, poor rate ability, and especially from a short lifespan, nearly losing their competitiveness over other battery systems. Herein, to accommodate huge K ions, we have designed favorable K-ion storage sites and diffusion pathways in a rigid host through crystal engineering and interface engineering, achieving high capacity ($\sim 205 \text{ mA h g}^{-1}$), superior rate ability ($\sim 72\%$ capacity retention at 8 A g^{-1}), and ultralong lifespan ($\sim 100\%$ capacity retention across nearly 10 000 cycles). These findings provide insights into host design for achieving fast K-ion storage and can be expanded as a universal strategy for creating electrode materials for other batteries, such as Mg-ion batteries and Zn-ion batteries.

^a Key Laboratory of Automobile Materials (Jilin University), Ministry of Education, Department of Materials Science and Engineering, Jilin University, Changchun 130022, China

^b State Key Laboratory of Rare Earth Resource Utilization, Changchun Institute of Applied Chemistry, Chinese Academy of Sciences, Changchun, 130022, P. R. China. E-mail: xbzhang@ciac.ac.cn

^c University of Science and Technology of China, Hefei, 230026, China

^d School of Materials Science and Engineering, Changchun University of Science and Technology, Changchun 130022, China

† Electronic supplementary information (ESI) available. See DOI: 10.1039/d1ee03924e

* These authors contributed equally.

Introduction

The increasing demand for sustainable energy storage is promoting research efforts toward developing new candidates beyond lithium-ion batteries (LIBs). The high cost of raw materials and limited Li reserves make LIBs unavailable to the stationary energy storage systems (ESS) that are needed for inexpensive and long-lasting batteries.^{1–3} Due to their potential cost-benefits and abundant resources, K-ion batteries (KIBs)

have recently garnered considerable attention as a promising candidate to support ESS.^{4–6} However, the K-ion size and coordination environments in host materials are significantly different from their Li counterparts. The insertion and diffusion of K ions into conventional electrode materials inevitably causes considerable structural stress and, to a large extent, causes electrochemical irreversibility.^{7–9} Efforts to improve the reversibility of KIBs have focused on modifying existing electrode materials used in LIBs and/or sodium-ion batteries (SIBs) or improving the electrode interface stability with electrolyte additives or artificially constructed protective interfaces.^{10–12} Nevertheless, the critical challenge stemming from the mismatched relationship between the large K ions and compact host structures has received scant attention.

The redox reactions for batteries mainly involve three mechanisms: intercalation/deintercalation, conversion, and alloying.⁹ Among them, the intercalation reactions that occur in layered metal oxides and polyanion compounds are considered to be the most facile way to accommodate large K ions because of the smallest structural strain–stress upon K-ion insertion/extraction.^{13–15} Generally, layered metal oxides consist of alternating slabs of metal oxides and alkali metal ions. Each pair of metal oxide layers are connected by weak van der Waals forces, thus forming 2D ionic channels wherein the cations can migrate.¹³ Theoretically, the expandable layered metal oxides are able to reversibly store large K ions through lattice expansion/contraction. However, the potassiated forms of layered metal oxides are thermodynamically unstable due to severe lattice distortion, causing significant capacity decay during cycles. Although the rational design of pillared systems might alleviate some of the structural failures upon repeated K-ion insertion/extraction,¹⁴ the structural cations that make up the pillars of the layered host will change the coordination environments for K ions, leading to an energetically unfavorable ion-insertion/diffusion process. Compared with layered metal oxides, polyanion compounds are characterized by high structural and thermodynamic stability due to their open frameworks connected by strong covalent bonds.¹⁵ Nevertheless, the rigid structure for polyanion compounds represents a double-edged sword, which enables a durable and reversible ion insertion/extraction process. But it simultaneously makes the diffusion of ions sluggish, particularly for large K ions, since the strong covalent bonds suppress structural rearrangement upon ion insertion. To accommodate large K ions reversibly, expandable structures are expected to relieve enormous structural stress upon K-ion insertion; on the other hand, rigid structures are required to guarantee long cycle stability. Therefore, it is a great challenge for one electrode material to achieve both high capacity and long cycle life in KIBs.

Layered KTiNbO_5 (KTNO) is considered an attractive host material to accommodate foreign species due to its unique layered structure with a large d -spacing of ~ 0.92 nm.^{16–18} Nevertheless, the insertion of large K ions into KTNO is considered problematic since the interlayer spaces for ion diffusion are occupied almost exclusively by the structural K ions that form the pillars of the layered structure. To create

favorable K-ion storage sites within the framework of KTNO, the structural K ions are either removed from the host or exchanged with other smaller cations to leave sufficient interstitial space. However, both Ti and Nb elements are in the forms of highest valence states, which cannot be oxidized, thereby making the extraction of structural K ions difficult, whether in a chemical or electrochemical oxidation process. Another way to approach this challenge is by substituting structural K ions with smaller cations *via* an ion-exchange strategy. For instance, exchanging K ions in KTNO with protons in acidic solutions generates layered HTiNbO_5 (HTNO).^{19,20} Compared with KTNO, the protonated form retains the original layered structure but has an enlarged interlayer space,¹⁹ theoretically providing favorable storage sites for K ions through 2D ionic channels. However, the Ti–Nb–O layers in HTNO are fixed by weak hydrogen bonds. It is difficult for such weak bonds to withstand the considerable structural stress upon repeated K-ion insertion. Theoretically, removing the structural protons in HTNO under an annealing process could induce the interconnections of two adjacent Ti–Nb–O layers by strong covalent bonds, thus forming tunnel-structured $\text{Ti}_2\text{Nb}_2\text{O}_9$ (TNO).^{21–23} The rigid TNO has a large tunnel along with an [010] orientation, which theoretically enable fast and stable storage/diffusion of K ions.

Herein, taking layered KTNO as an example, we illustrate our reasonable assumptions through proof-of-concept experiments and density functional theory (DFT) calculations. We synthesized various titanoniobates, including KTNO, HTNO, and TNO, through a series of topological reactions. Compared with layered KTNO and HTNO, the tunnel-structured TNO provides robust diffusion channels that allow fast diffusion of large K ions in a zero-strain way, which is verified by both electrochemical tests and theoretical calculation. To further overcome the limitation of K-ion storage sites inside a crystal, we designed and synthesized carbon-coated and sandwich-like TNO nanosheets (CTNO). The resultant heterogeneous interfaces between the carbon layer and TNO nanosheets compensate for the unsaturated coordination environment of the TNO external surface and consequently provide abundant K-ion storage sites. Thanks to its topological structure and interface optimization, the as-prepared CTNO exhibits superior K-storage performance in terms of capacity (~ 205 mA h g^{-1}), rate capability ($\sim 72\%$ capacity retention at 8 A g^{-1}), and cycle stability ($\sim 100\%$ capacity retention across nearly 10 000 cycles), which overcome the cycle limitation of KIBs.

Results and discussion

The KTNO, HTNO, and TNO unit cell structures are presented in Fig. 1a and Fig. S1 (ESI[†]). Typically, KTNO has a layered structure that contains corner- and edge-sharing octahedral units of TiO_6 and NbO_6 and the interbedded K atom, which form a unique open frame with a large d -spacing of ~ 0.92 nm.¹⁷ In contrast, HTNO retains a layered structure with its d -spacing decreased to ~ 0.84 nm.²⁰ Notably, every pair

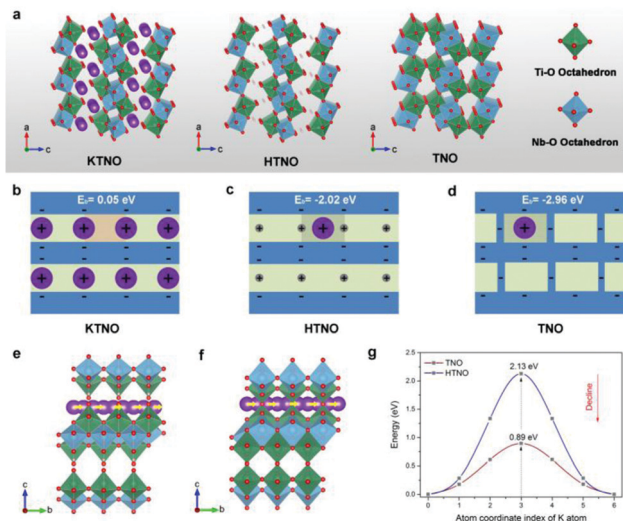


Fig. 1 DFT calculation for screening the favorable sites for K-ion storage. (a) Crystal structure models of KTNO, HTNO, and TNO. (b–d) Schematic illustrations of the (020) crystal planes for KTNO, HTNO, and TNO and the corresponding binding energies for one K ion in the hosts. (e–g) The diffusion diagrams of K ions in HTNO (e) and TNO (f) along the [010] direction and the corresponding diffusion energy barriers (g).

of successive layers in HTNO are interconnected by weak hydrogen bonds, which may be broken upon K ion insertion due to the considerable structural stress. Unlike KTNO and HTNO, TNO possesses a tunnel structure with large voids encompassed by the octahedral units of TiO_6 or NbO_6 ,^{21–23} which possibly allow fast K-ion storage in 1D ionic channels along the [010] direction. Meanwhile, the tunnel-structured TNO may be robust enough to accommodate the huge structural stress upon repeated K-ion (de)intercalation due to the strong atomic bond connecting every pair of layers.

To verify the above assumptions, we investigated the binding and diffusion behavior of the K ion in KTNO, HTNO, and TNO by first-principles calculations (Fig. 1b–g, Fig. S2–S4, ESI†). The binding energy (E_b) for one K ion in TNO reaches the lowest value of -2.96 eV (Fig. 1b–d). As we know, a more negative value of E_b indicates a more energetically favorable reaction.²⁴ Therefore, the insertion of K ions into TNO is thermodynamically more feasible, and the inserted form of TNO is more stable than those of KTNO and HTNO. Notably, potassiated KTNO is thermodynamically unstable (pronounced lattice distortions are detected in Fig. S2a (ESI†) after one K-ion insertion) due to its E_b (0.05 eV) being greater than zero.²⁵ The rate performance of KIBs is mainly determined by K ion mobility in the electrode material. We then employed the climbing image nudged elastic band (CI-NEB) method to quantify the diffusion of a K atom in HTNO (Fig. 1e and Fig. S3, ESI†) and TNO (Fig. 1f and Fig. S4, ESI†) along the [010] direction.²⁶ Notably, the diffusion energy barrier of K ions in TNO is calculated to be 0.89 eV, which is much lower than that of HTNO (2.13 eV), demonstrating that the diffusion of K ions in TNO is kinetically faster than in HTNO (Fig. 1g). These simulation results confirm that TNO is an excellent K-storage

material with energetically favorable K-storage sites and diffusion channels.

As proof-of-concept experiments, various titanoniobates, including KTNO, HTNO, and TNO, were synthesized *via* a series of topological reactions (Fig. S5, ESI†). Specifically, layered KTNO crystals were synthesized from stoichiometric amounts of K_2CO_3 , TiO_2 , and Nb_2O_5 by a high-temperature solid-phase reaction.¹⁶ Subsequently, the protonated form of HTNO was prepared by a proton exchange reaction between KTNO and HCl aqueous solution.^{19,20} Finally, an annealing treatment at 450°C realized the topological transition from HTNO to TNO.^{21–23} XRD patterns (Fig. S6 and S7, ESI†) and XPS results (Fig. S8, ESI†) demonstrated the successful synthesis of KTNO, HTNO, and TNO. And all three examples were composed of tabular particles of up to several micrometers (Fig. S9, ESI†). It should be highlighted that the similar morphologies of KTNO, HTNO, and TNO could eliminate the difference in battery performance caused by different morphologies.

The electrochemical performances of KTNO, HTNO, and TNO towards potassium were investigated using coin cells with metallic K as the counter electrode (Fig. 2a and d). However, HTNO proved to be unstable in KIBs before the electrochemical test since its crystal structure changes after immersion into electrolyte for a few hours (Fig. S10, ESI†). We assume that the structural evolution from HTNO to KTNO is probably caused by spontaneous ion exchange between protons and K ions. Galvanostatic charge/discharge techniques were then used to evaluate the electrochemical performances of KTNO and TNO at a

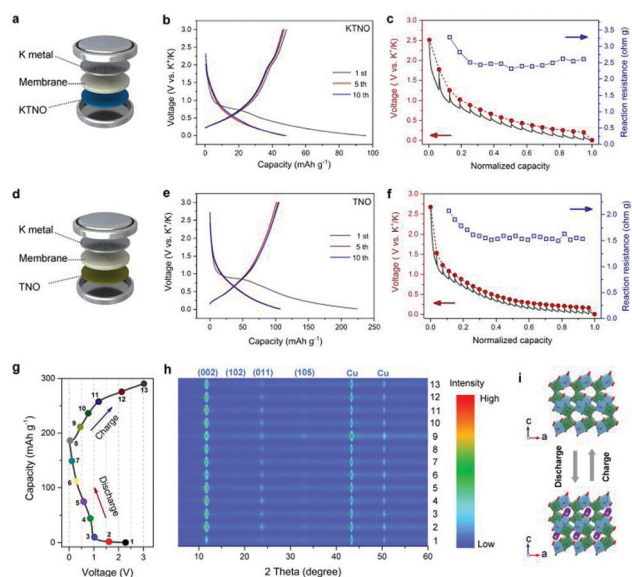


Fig. 2 K-storage behavior of KTNO and TNO. (a) and (b) The battery structure diagram and galvanostatic charge/discharge curves of KTNO at a current density of 50 mA g^{-1} . (c) GITT curve and the corresponding reaction resistance of KTNO at a current density of 50 mA g^{-1} . (d) and (e) The battery structure diagram and galvanostatic charge/discharge curves of TNO at a current density of 50 mA g^{-1} . (f) GITT curve and the corresponding reaction resistance of TNO at a current density of 50 mA g^{-1} . (g) and (h) XRD profiles of TNO at different charge and discharge states. (i) Structural evolution of TNO upon K ion insertion/extraction.

current density of 50 mA g^{-1} . As shown in Fig. 2b, the as-prepared KTNO delivers initial discharge and charge capacities of ~ 96 and $\sim 49 \text{ mA h g}^{-1}$, respectively, with a Coulombic efficiency of 51% in the first cycle. The irreversible capacities are attributed to the formation of a solid–electrolyte interphase (SEI) and partially irreversible insertion of K ions.^{27–29} In the subsequent cycles, the KTNO electrode exhibits excellent cycling stability without distinct capacity decay. Compared with KTNO, TNO electrodes deliver a higher reversible capacity of $\sim 105 \text{ mA h g}^{-1}$, roughly doubling the capacity of KTNO (Fig. 2e). This meant that the topological deformation from KTNO to TNO created more K-ion storage sites in the host framework. In addition, the overlapping voltage profiles of TNO demonstrate its excellent electrochemical reversibility.

Galvanostatic intermittent titration technique (GITT) measurement was employed to determine the diffusion kinetics of K-ions in KTNO and TNO (application of a series of current pulses at 50 mA g^{-1} for 5 min followed by resting for another 30 min).^{30–32} Reaction resistances (overpotential divided by the pulse current density) calculated from GITT curves were used to measure the reaction kinetics in the KTNO and TNO electrodes.³³ In KTNO, the reaction resistance decreases from an initial value of $\sim 3.5 \Omega \text{ g}$ to a stable value of $\sim 2.5 \Omega \text{ g}$ (Fig. 2c). As expected, TNO demonstrates lower reaction resistance than KTNO, which shows a stable reaction resistance of $\sim 1.5 \Omega \text{ g}$ as the insertion reaction progresses (Fig. 2f). These results are consistent with the calculation results, demonstrating enhanced reaction kinetics in such a framework after topological optimization.

Noticeably, the charge/discharge curves of TNO are completely sloping; it appears that there is a solid–solution type process instead of a phase separation reaction upon K-ion (de)intercalation.^{34–36} This characteristic is further verified by the *ex situ* XRD patterns (Fig. 2g and h) and the structural evaluations (Fig. 2i) of the TNO electrode, since the XRD patterns for the TNO electrode remain almost unchanged at different discharge and charge stages. Enlarged XRD patterns of the TNO electrode reveal that the *d*-spacing along the *c* direction increases from 7.44 \AA to 7.45 \AA upon K-ion insertion and totally recovers upon K-ion extraction (Fig. S11, ESI†). The small volume expansion suggests a zero-strain characteristic for TNO, which ensures a potentially long cycle life. In contrast, KTNO suffers relatively larger volume expansion upon K-ion insertion/extraction (Fig. S12, ESI†), although it delivers lower capacity.

To overcome the limitation of K-ion storage sites inside TNO, CTNO has been constructed *via* liquid exfoliation of HTNO followed by thermal dehydration, as illustrated in Fig. 3a. Specifically, HTNO is first mixed with the intercalator of tetrabutylammonium hydroxide (TBAOH) solution to introduce bulky organic ions (TBA^+) into its interlayers. The insertion of voluminous TBA^+ cations expands the interlayer spacing and breaks the van der Waals forces between each layer, leading to the exfoliation of HTNO. The exfoliated white metal oxide nanosheets (NSs) are then heat-treated at $450 \text{ }^\circ\text{C}$ to produce black CTNO (Fig. S13, ESI†). Unlike bulk TNO with

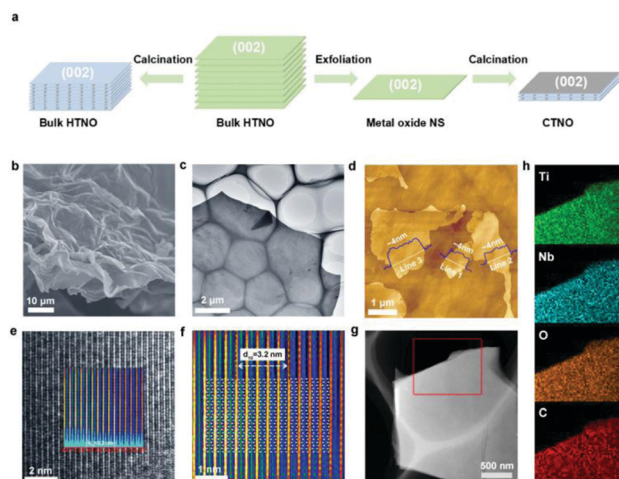


Fig. 3 Structural and morphological characterization of CTNO. (a) Schematic illustration of the formation of CTNO. (b–e) SEM (b), TEM (c), AFM (d) and HRTEM (e) images of CTNO. (f) IFFT image and the corresponding structural model of CTNO on the (002) plane. (g, h) HAADF STEM (g) image and EDS elemental mappings (h) of Ti, Nb, O, and C in the selected region indicated by the red rectangle in (g).

its plate-like shape, the as-prepared CTNO shows a large-area 2D sheet-like morphology (Fig. 3b and c) with an average thickness of $\sim 4 \text{ nm}$ (Fig. 3d). XRD pattern and XPS results confirm that the composition and crystal structure of CTNO are the same as those of TNO (Fig. S14 and S15, ESI†). Note that the weak and broad diffraction peaks of CTNO are detected in Fig. S14 (ESI†), which may be due to its nanosheet morphology with poor crystallization. HRTEM images of the nanosheets show a lattice fringe of 3.2 \AA (Fig. 3e), corresponding to the interlayer distance of the (200) planes of the orthorhombic TNO phase. Fig. 3f shows the inverse Fast Fourier Transform (IFFT) images from the areas in the frames of Fig. 3e. The atomic arrangements in the IFFT image are consistent with typical atomic configurations of the orthorhombic TNO phase projected along the [001] direction. These results indicate that the CTNO nanosheets have a (002) crystal plane orientation. Fig. 3g and h display the high-angle annular dark-field scanning TEM (HAADF STEM) image and corresponding energy-dispersive X-ray spectroscopy (EDS) map of CTNO. Notably, the carbon element is detected in EDS elemental mapping data with the homogeneous distribution along the nanosheets. Since the TBA^+ cations are adsorbed on the surface of the metal oxide nanosheets after the liquid exfoliation process, the decomposition of the TBA^+ cations during the thermal dehydration process is probably responsible for the formation of the carbon-coated layer. Additionally, Raman spectra confirm that the carbon signal originated from the highly graphitized carbon with an IG/ID of 1.3 (Fig. S16, ESI†),³⁷ and thermogravimetric analysis (TG) shows that the carbon content in CTNO is 12.5% (Fig. S17, ESI†). It should be highlighted that the highly graphitized carbon layer could improve the electrical conductivity and structural stability of the TNO nanosheets, in turn realizing high-rate and long-cycle stable battery performance.

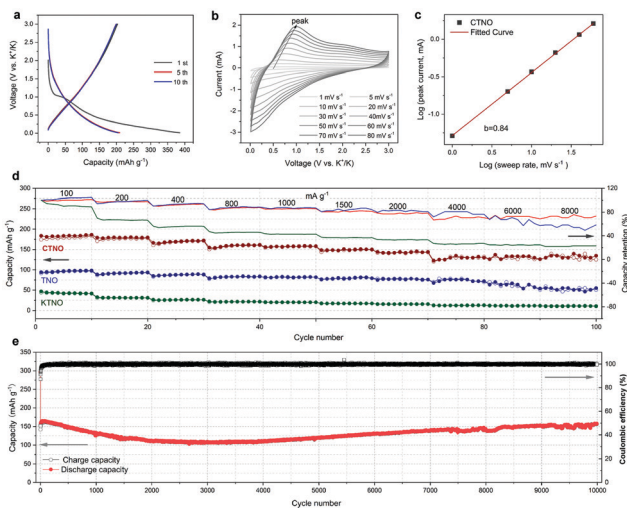


Fig. 4 K-storage performance of CTNO. (a) galvanostatic charge/discharge curves of CTNO at a current density of 50 mA g^{-1} . (b) CV curves of CTNO at various scan rates from 1 to 80 mV s^{-1} . (c) Calculation of b -values from the relationship between the scan rate and peak current in (b). (d) Rate capability and corresponding discharge capacity retention for KTNO, TNO, and CTNO at various current densities of 100 to 8000 mA g^{-1} . (e) Cycle performance of CTNO at a current density of 1000 mA g^{-1} .

The electrochemical performances of CTNO towards potassium were investigated using coin cells with metallic K as the counter electrode. As shown in Fig. 4a, CTNO delivers a reversible capacity of $\sim 205 \text{ mA h g}^{-1}$, roughly doubling the capacity of TNO. And the discharge plateau at $\sim 0.90 \text{ V}$, also observed in the first voltage profiles of KTNO and TNO, can probably be attributed to the formation of SEL.³⁰ To reveal the reasons behind the performance improvement, sweep-rate-dependent cyclic voltammetry (CV) measurements were applied to investigate the kinetics and charge storage mechanism of KTNO and TNO. The CV curves of the CTNO electrode at different scan rates are presented in Fig. 4b. The broad peaks correspond well to the galvanostatic charge/discharge profiles, further demonstrating its solid-solution behavior. It should be noted that the broad peaks are retained and significantly enhanced in all CV curves with a scan rate from 1 to 80 mV s^{-1} . Theoretically, the current (i) and sweep rates (v) obey the following formula:³⁸

$$i = av^b \quad (1)$$

where a and b are two variable values, and the b -value could be determined by the $\log(v)$ slope against $\log(i)$ plots. Generally, a b -value of 1.0 represents a capacitance-dominated process, while a b -value of 0.5 indicates a diffusion-controlled process.³⁹ As shown in Fig. S18 (ESI[†]), the b -value for the TNO electrode is calculated to be 0.70, suggesting a combination of the surface charge storage process with the diffusion-limited charge-storage process. In contrast, the b -value for the CTNO electrode is 0.84 (Fig. 4c); the higher b -value demonstrates the enhanced capacitive behavior, which is probably responsible for the improved K-storage performance. Fig. 4d shows the rate capabilities of the three electrodes at various

current densities (100 to 8000 mA g^{-1}). Among them, CTNO exhibits a remarkable property with its capacity retention better than those of KTNO or TNO over the current densities. In particular, the capacity retention of CTNO reaches a value of $\sim 72\%$ ($\sim 133 \text{ mA h g}^{-1}$) at an extremely high rate of 8000 mA g^{-1} . Furthermore, CTNO exhibits excellent cycle stability with the longest cycle life and the highest capacity retention rate, whether at low (100 mA g^{-1} ; Fig. S19, ESI[†]) or high current density (1000 mA g^{-1} ; Fig. 4e and Fig. S20, ESI[†]). Remarkably, CTNO displays a lifespan of nearly 10 000 cycles without capacity fading (Fig. 4e), which is significantly better than that of current state-of-the-art electrodes in KIBs (Fig. S21 and Table S1, ESI[†]).^{40–42}

But CTNO has a smaller thickness ($\sim 4 \text{ nm}$) along the [001] direction compared with TNO (average size $\sim 600 \text{ nm}$; Fig. 5a, b, and Fig. S22, ESI[†]). Decreasing the particle size of TNO along the [001] direction does not seem to shorten the diffusion distance for K ions, as the diffusion process occurs in the a - b plane. Thus, the nanosheet-like morphology of TNO may not be the main reason for its improved rate performance. The exposed (002) planes in CTNO have been proven to be coated by graphitized carbon; the heterogeneous interfaces created between the carbon layer and TNO may be another host site for the accommodation of K ions.

To test the hypothesis, we then employed simplified graphene-TNO structural models (Fig. S23, ESI[†]) to investigate the electrical conductivity and K-ion adsorption/diffusion behavior of CTNO. Density of states (DOS) was performed to study the electrical properties of TNO and graphene-TNO.⁴³ From the DOS differences at the Fermi level (Fig. S24, ESI[†]), graphene-TNO shows significantly improved electrical conductivity compared with pure TNO due to the energy gap contraction.⁴³ Additionally, the binding energy of a single K atom in the heterogeneous interfaces in graphene-TNO is calculated to be -4.84 eV (Fig. 5c), which is more negative than that in TNO (-2.96 eV). The charge-density differences further confirm the enhanced K adsorption ability in CTNO. As shown in Fig. 5c, the electrons accumulate in the intermediate region between the K atom and graphene, which accounts for the improved binding energy.⁴⁴ The diffusion energy barriers for K ions through the heterogeneous interface in graphene-TNO were also investigated. Compared with TNO, graphene-TNO demonstrates a lower diffusion energy barrier of 0.54 eV along the

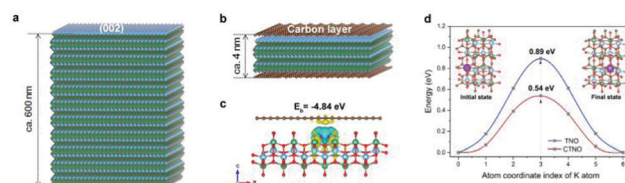


Fig. 5 DFT calculation reveals the K-ion diffusion behavior in CTNO. (a,b) Schematic diagram of bulk TNO (a) and CTNO (b). (c) Charge density difference with one K atom adsorbed for CTNO; green and yellow represent charge loss and accumulation, respectively. (d) The diffusion energy barrier of K ions in TNO and CTNO along the [010] direction.

[010] direction (Fig. 5d and Fig. S25, ESI†). These calculation results confirm that the incorporation of carbon favorably enhances the electrical conductivity of TNO and provides extra K-storage sites with lower diffusion energy barriers in the heterogeneous interfaces, which are responsible for the better K-storage performance.

Conclusions

In summary, to counter the mismatched relationship between large K ions and compact host structures, we first constructed a rigid tunnel-structured TNO derived from layered KTNO through topological transformation, which allows fast storage and diffusion of K ions within its 1D ionic channels in a zero-strain way. Additionally, to overcome the limitation of K-ion storage sites inside the crystal, TNO was then exfoliated into nanosheets and further coated with a highly graphitized carbon layer. The resultant heterogeneous interfaces compensate for the unsaturated coordination environment of the TNO external surface and consequently provide abundant K-ion storage sites. As a result, CTNO exhibits high reversible capacity ($\sim 205 \text{ mA h g}^{-1}$), excellent rate capability ($\sim 72\%$ capacity retention at 8 A g^{-1}), and remarkable lifespan ($\sim 100\%$ capacity retention across nearly 10 000 cycles). Our strategy provides insight into host design for accommodating large parasitic ions from the adaptation relationship between hosts and inserted ions. And it could be expanded as a general strategy for creating electrode materials for other batteries.

Author contributions

X.-B. Z. and Y.-H. Z. developed the concept. Y.-H. Z. carried out the electrochemical experiment. J.-Z. W. and Q. Z. performed the first-principles calculations. Y.-H. Z. and X.-B. Z. wrote the paper. Y.-H. Z., Y.-F. C., G. H., J.-M. Y., and X.-B. Z. participated in the analysis of the experimental data, discussion of the results, and preparation of the paper.

Conflicts of interest

There are no conflicts to declare.

Acknowledgements

This work is financially supported by the National Natural Science Foundation of China (21725103, 51522101, 51471075, 51631004, and 51401084), China Postdoctoral Science Foundation (2020M681035), Key Research Program of the Chinese Academy of Sciences (ZDRW-CN-2021-3-3), and K. C. Wong Education Foundation (GJTD-2018-09).

Notes and references

1 B. Dunn, H. Kamath and J. M. Tarascon, *Science*, 2011, **334**, 928–935.

- 2 C. D. Wessells, R. A. Huggins and Y. Cui, *Nat. Commun.*, 2011, **2**, 550.
- 3 O. Schmidt, A. Hawkes, A. Gambhir and I. Staffell, *Nat. Energy*, 2017, **2**, 17110.
- 4 H. Wang, D. Zhai and F. Kang, *Energy Environ. Sci.*, 2020, **13**, 4583–4608.
- 5 M. Zhou, P. X. Bai, X. Ji, J. X. Yang, C. S. Wang and Y. H. Xu, *Adv. Mater.*, 2020, **33**, 2003741.
- 6 W. Zhang, Y. Liu and Z. Guo, *Sci. Adv.*, 2019, **5**, 7412.
- 7 R. Rajagopalan, Y. Tang, X. Ji, C. Jia and H. Wang, *Adv. Funct. Mater.*, 2020, **30**, 1909486.
- 8 X. Min, J. Xiao, M. Fang, W. A. Wang, Y. Zhao, Y. Liu, A. M. Abdelkader, K. Xi, R. V. Kumar and Z. Huang, *Energy Environ. Sci.*, 2021, **14**, 2186–2243.
- 9 J. Y. Hwang, S. T. Myung and Y. K. Sun, *Adv. Funct. Mater.*, 2018, **28**, 1802938.
- 10 W. Zhang, Y. Liu and Z. Guo, *Sci. Adv.*, 2019, **5**, eaav7412.
- 11 R. Zhang, J. Bao, Y. Pan and C. F. Sun, *Chem. Sci.*, 2019, **10**, 2604–2612.
- 12 S. Liu, J. Mao, Q. Zhang, Z. Wang, W. K. Pang, L. Zhang, A. Du, V. Sencadas, W. Zhang and Z. Guo, *Angew. Chem., Int. Ed.*, 2020, **59**, 3638–3644.
- 13 Z. Liu, H. Su, Y. Yang, T. Wu, S. Sun and H. Yu, *Energy Storage Mater.*, 2021, **34**, 211–228.
- 14 B. Tian, W. Tang, C. Su and Y. Li, *ACS Appl. Mater. Interfaces*, 2018, **10**, 642–650.
- 15 J. Huang, X. Cai, H. Yin, Y. Li, W. Lin, S. Huang and Y. Zhang, *J. Phys. Chem. Lett.*, 2021, **12**, 2721–2726.
- 16 A. D. Wadsley, *Acta Crystallogr.*, 1964, **17**, 623–628.
- 17 G. H. Du, Y. Yu, Q. Chen, R. H. Wang, W. Zhou and L. M. Peng, *Chem. Phys. Lett.*, 2003, **377**, 445–448.
- 18 S. Chausson, V. Caignaert, R. Retoux, J. M. Rueff, L. Le Pluart, P. J. Madec and P. A. Jaffrès, *Polymer*, 2008, **49**, 488–496.
- 19 A. Takagaki, M. Sugisawa, D. Lu, J. N. Kondo, M. Hara, K. Domen and S. Hayashi, *J. Am. Chem. Soc.*, 2003, **125**, 5479–5485.
- 20 H. Park, J. Kwon, H. Choi, T. Song and U. Paik, *Sci. Adv.*, 2017, **3**, e1700509.
- 21 J. F. Colin, V. Pralong, M. Hervieu, V. Caignaert and B. Raveau, *Chem. Mater.*, 2008, **20**, 1534–1540.
- 22 L. Shen, Y. Wang, H. Lv, S. Chen, P. A. van Aken, X. Wu, J. Maier and Y. Yu, *Adv. Mater.*, 2018, **30**, 1804378.
- 23 M. Fang, C. H. Kim and T. E. Mallouk, *Chem. Mater.*, 1999, **11**, 1519–1525.
- 24 W. Li, Y. Yang, G. Zhang and Y. W. Zhang, *Nano Lett.*, 2015, **15**, 1691–1697.
- 25 D. Koch, V. V. Kulish and S. Manzhos, *MRS Commun.*, 2017, **7**, 819–825.
- 26 G. Henkelman, B. P. Uberuaga and H. Jónsson, *J. Chem. Phys.*, 2000, **113**, 9901–9904.
- 27 Y. Lei, D. Han, J. Dong, L. Qin, X. Li, D. Zhai, B. Li, Y. Wu and F. Kang, *Energy Storage Mater.*, 2020, **24**, 319–328.
- 28 Y. Xie, Y. Chen, L. Liu, P. Tao, M. Fan, N. Xu, X. Shen and C. Yan, *Adv. Mater.*, 2017, **29**, 1702268.
- 29 X. Wu, W. Zhao, H. Wang, X. Qi, Z. Xing, Q. Zhuang and Z. Ju, *J. Power Sources*, 2018, **378**, 460–467.

- 30 D. W. Dees, S. Kawauchi, D. P. Abraham and J. Prakash, *J. Power Sources*, 2009, **189**, 263–268.
- 31 J. Xie, N. Imanishi, A. Hirano, Y. Takeda, O. Yamamoto, X. B. Zhao and G. S. Cao, *Solid State Ionics*, 2010, **181**, 1611–1615.
- 32 K. Tang, X. Yu, J. Sun, H. Li and X. Huang, *Electrochim. Acta*, 2011, **56**, 4869–4875.
- 33 J. Zhao, X. Zou, Y. Zhu, Y. Xu and C. Wang, *Adv. Funct. Mater.*, 2016, **26**, 8103–8110.
- 34 S. M. Xu, Y. C. Ding, X. Liu, Q. Zhang, K. X. Wang and J. S. Chen, *Adv. Energy Mater.*, 2018, **8**, 1802175.
- 35 C. Bommier, T. W. Surta, M. Dolgos and X. Ji, *Nano Lett.*, 2015, **15**, 5888–5892.
- 36 K. Cao, H. Liu, W. Li, C. Xu, Q. Han, Z. Zhang and L. Jiao, *J. Electroanal. Chem.*, 2019, **841**, 51–55.
- 37 Y. Xu, L. Zhu, X. Cui, M. Zhao, Y. Li, L. Chen, W. Jiang, T. Jiang, S. Yang and Y. Wang, *Nano Res.*, 2020, **13**, 752–758.
- 38 Y. Shao, M. F. El-Kady, J. Sun, Y. Li, Q. Zhang, M. Zhu, H. Wang, B. Dunn and R. B. Kaner, *Chem. Rev.*, 2018, **118**, 9233–9280.
- 39 Y. Dou, D. Yuan, D. Adekoya, Y. Tian, S. Adekoya, L. Xu and S. Zhang, *Angew. Chem., Int. Ed.*, 2021, **133**, 18978–18985.
- 40 J. C. Pramudita, D. Sehwat, D. Goonetilleke and N. Sharma, *Adv. Energy Mater.*, 2017, **7**, 1602911.
- 41 H. Kim, J. C. Kim, M. Bianchini, D. H. Seo, J. Rodriguez-Garcia and G. Ceder, *Adv. Energy Mater.*, 2018, **8**, 1702384.
- 42 J. Y. Hwang, S. T. Myung and Y. K. Sun, *Adv. Funct. Mater.*, 2018, **28**, 1802938.
- 43 P. Larsson, R. Ahuja, A. Nytén and J. O. Thomas, *Electrochem. Commun.*, 2006, **8**, 797–800.
- 44 B. Chen, H. Li, H. Liu, X. Wang, F. Xie, Y. Deng, W. Hu, K. Davey, N. Zhao and S. Z. Qiao, *Adv. Energy Mater.*, 2019, **9**, 1901146.